

Exploring Dark Matter with Milky Way substructure

Michael Kuhlen^{1*}, Piero Madau², Joseph Silk³

¹School of Natural Sciences, Institute for Advanced Study, Princeton, NJ 08540

²Department of Astronomy & Astrophysics, University of California, Santa Cruz, CA 95064

³Department of Physics, University of Oxford, Oxford, OX1 3RH, UK

The unambiguous detection of Galactic dark matter annihilation would unravel one of the most outstanding puzzles in particle physics and cosmology. Recent observations have motivated models in which the annihilation rate is boosted by the Sommerfeld effect, a non-perturbative enhancement arising from a long range attractive force. Here we apply the Sommerfeld correction to *Via Lactea II*, a high resolution N -body simulation of a Milky-Way-size galaxy, to investigate the phase-space structure of the Galactic halo. We show that the annihilation luminosity from kinematically cold substructure can be enhanced by orders of magnitude relative to previous calculations, leading to the prediction of γ -ray fluxes from up to hundreds of dark clumps that should be detectable by the *Fermi* satellite.

In the standard cold dark matter (CDM) paradigm of structure formation, a weakly interacting massive particle (WIMP) of mass $m_\chi \sim 100$ GeV-10 TeV ceases to annihilate when the universe cools to a temperature of $T_f \sim m_\chi/20$, about one nano-second after the Big Bang. A thermally-averaged cross-section at freeze-out of $\langle\sigma v\rangle_0 \approx 3 \times 10^{-26}$ cm³ s⁻¹ results in a relic abundance consistent with observations (1). Perturbations in the dark matter density are amplified by gravity after the universe becomes matter dominated, around ten thousand years after the Big Bang: the smallest structures (“halos”) collapse earlier when the universe is very dense and merge to form larger and larger systems over time. Today, galaxies like our own Milky Way are embedded in massive, extended halos of dark matter that are very lumpy, teeming with self-bound substructure (“subhalos”) that survived this hierarchically assembly process (2–4). Indirect detection of high energy antiparticles and γ -rays from dark matter halos provides a potential “smoking gun” signature of WIMP annihilation (5). The usual assumption that WIMP annihilation proceeds at a rate that does not depend, in the non-relativistic $v/c \ll 1$ limit, on

*To whom correspondence should be addressed; E-mail: mqk@ias.edu.

the particle relative velocities implies that the primary astrophysical quantity determining the annihilation luminosity today is the local density squared. WIMP annihilations still occur in the cores of individual substructures, but with fluxes that are expected to be dauntingly small. The latest calculations show that only a handful of the most massive Galactic subhalos may, in the best case, be detectable in γ -rays by the *Fermi* satellite (6, 7).

The Sommerfeld enhancement, a velocity-dependent mechanism that boosts the dark matter annihilation cross-section over the standard $\langle\sigma v\rangle_0$ value (8–11), may provide an explanation for the experimental results of the PAMELA satellite reporting an increasing positron fraction in the local cosmic ray flux at energies between 10 and 100 GeV (12), as well as for the surprisingly large total electron and positron flux measured by the ATIC and PPB-BETS balloon-borne experiments (13, 14). Very recent Fermi (15) and H.E.S.S. (16) data appear to be inconsistent with the ATIC and PPB-BETS measurements, but still exhibit departures with respect to standard expectations from cosmic ray propagation models. Although conventional astrophysical sources of high energy cosmic rays, such as nearby pulsars or supernova remnants, may provide a viable explanation (17–19), the possibility of Galactic DM annihilation as a source remains intriguing (20–22). In this case, cross-sections a few orders of magnitude above what is expected for a thermal WIMP are required (23).

The Sommerfeld non-perturbative increase in the annihilation cross-section at low velocities is the result of a generic attractive force between the incident dark matter particles that effectively focuses incident plane-wave wavefunctions. The force carrier may be the W or Z boson of the weak interaction (10), $m_\phi = 80 - 90 \text{ GeV}/c^2$, or a lighter boson, $m_\phi \sim \text{GeV}/c^2$, mediating a new interaction in the dark sector (11, 24). Upon introduction of a force with coupling strength α , the annihilation cross-section is shifted to $\langle\sigma v\rangle = S\langle\sigma v\rangle_0$, where the Sommerfeld correction S disappears ($S = 1$) in the limit $v/c \rightarrow 1$ (thus leaving unchanged the weak scale annihilation cross-section during WIMP freeze-out in the early universe). When $v/c \ll \alpha$, $S \approx \pi\alpha c/v$ (“ $1/v$ ” enhancement), but it levels off to $S_{\text{max}} \approx 6\alpha m_\chi/m_\phi$ at $v/c \approx 0.5m_\phi/m_\chi$ because of the finite range of the interaction. For specific parameter combinations, i.e. when $m_\chi/m_\phi \approx n^2/\alpha$ where n is an integer, the (Yukawa) potential develops bound states, and these give rise to large, resonant cross-section enhancements where S grows approximately as $1/v^2$ before saturating (see Supporting Online Material).

The Sommerfeld effect connects dynamically the dark and the astrophysics sectors. Because the typical velocities of dark matter particles in the Milky Way today are of the order of $v/c \sim 10^{-3}$, the resulting boost in the annihilation rate may provide an explanation to the puzzling Galactic signals. Compared to particles in the smooth halo component, the Sommerfeld correction preferentially enhances the annihilation luminosity of cold, lower velocity dispersion substructure, as emphasized previously by (10, 25, 26). Detailed knowledge of the full phase-space density of dark matter particles in the Milky Way is thus necessary to reliably compute the expected signals. Here we use the *Via Lactea II* cosmological simulation, a high precision calculation of the assembly of the Galactic CDM halo, for a systematic investigation of the impact of Sommerfeld-corrected models on present and future indirect dark matter detection efforts. *Via Lactea II* employs just over one billion $4,100 M_\odot$ particles to follow, with a

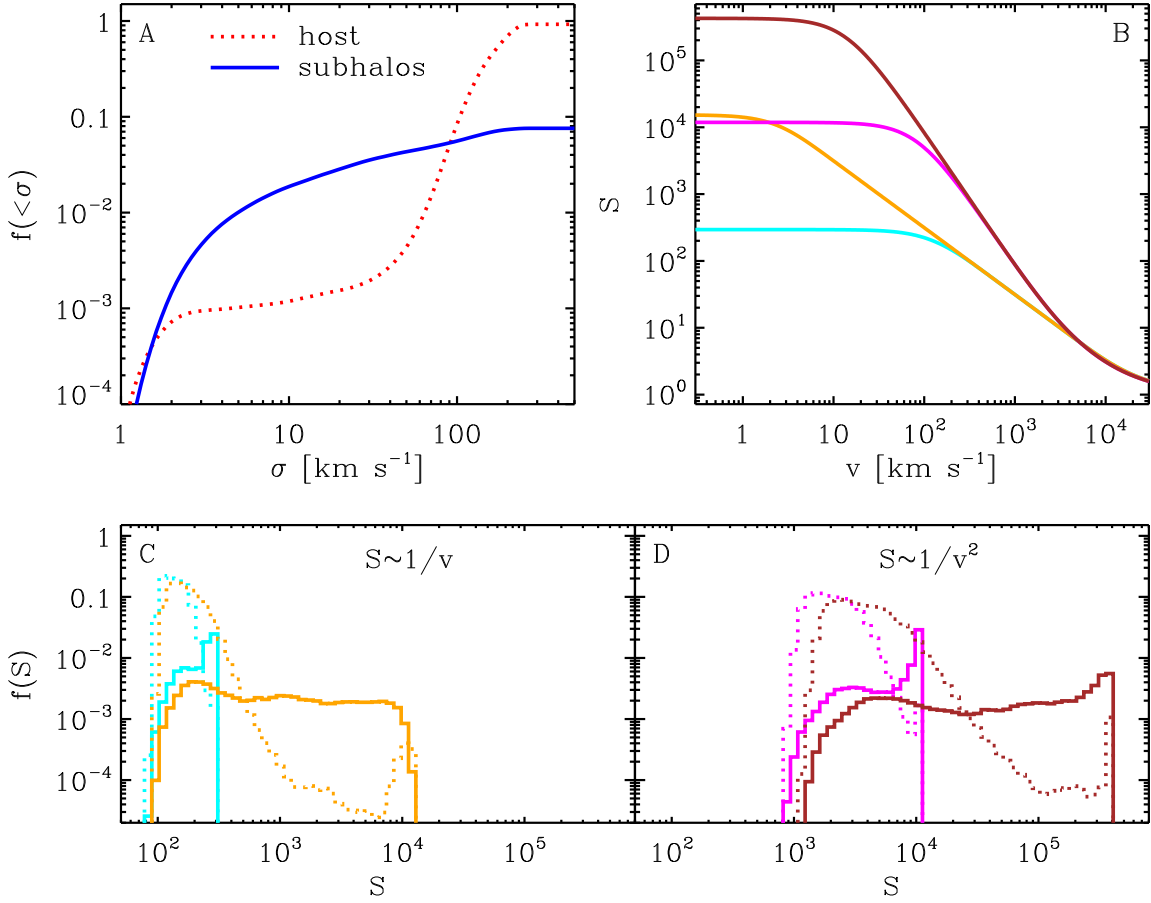


Figure 1: A: The distribution of velocity dispersion for *Via Lactea II* particles within 400 kpc. The dispersions are calculated from the nearest 32 neighbors of each particle. B: Sommerfeld enhancement factor as a function of velocity for four representative models, exhibiting $S \sim 1/v$ (cyan and orange curves) and $\sim 1/v^2$ behavior (magenta and brown), and high (cyan and magenta) versus low (orange and brown) saturation velocities. C and D: The corresponding distributions of S-factors for *Via Lactea II* particles.

force resolution of 40 pc, the formation of a $1.9 \times 10^{12} M_{\odot}$ Milky-Way size halo and its substructure from redshift $z = 104$ to the present (27–29). (Fig. 1 A) The smooth halo particles, whose velocity dispersions are set by the global potential, typically have three-dimensional velocity dispersion $\sigma > 100 \text{ km s}^{-1}$. Particles in self-bound subhalos dominate at lower velocity dispersions. The total mass fraction of particles with $\sigma < 5 \text{ km s}^{-1}$ is 1%. We calculated the Sommerfeld enhancement factors S on a particle-by-particle basis by averaging $S(v)$ over a Maxwell-Boltzmann distribution of relative velocities with one-dimensional velocity dispersion given by $\sqrt{2/3} \sigma$ (see the Supporting Online Materials for details) (Fig. 1 C, D).

The large Sommerfeld boost expected for $v/c \sim 10^{-4} - 10^{-5}$ make cold subhalos more promising sources of annihilation γ -rays than the higher density but much hotter region around

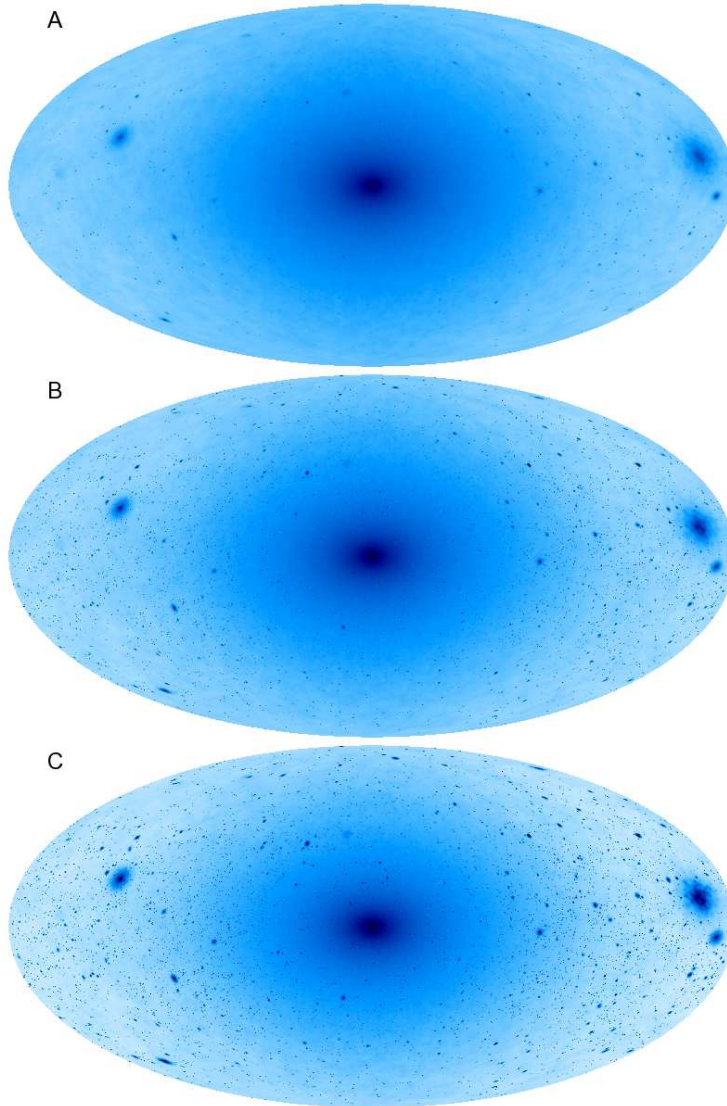


Figure 2: All-sky maps (in a Mollweide projection) of the Sommerfeld-enhanced annihilation surface brightness ($\int_{\text{los}} \rho^2 S \, d\ell$) from all *Via Lactea II* dark matter particles within 400 kpc. The observer is located at 8 kpc from the halo center along the host halo’s intermediate principal axis. A: No Sommerfeld enhancement. B: $S \sim 1/v$, saturated at $\sim 1 \text{ km s}^{-1}$. C: $S \sim 1/v^2$ saturated at $\sim 5 \text{ km s}^{-1}$. The maps have been normalized to give the same total smooth host halo flux.

the Galactic Center (Fig. 2). In Sommerfeld-enhanced models, substructures are much more clearly visible, and can even outshine the Galactic Center when the cross-section is close to resonance and saturates at low velocities. Furthermore, baryonic processes will tend to heat up the Galactic Center and dim its Sommerfeld boost, and thereby increase the relative detectability of subhalos. Dark matter halos are not isothermal and have smaller velocity dispersions in the center (see Supporting Online Material). In addition to an overall increase in the annihilation

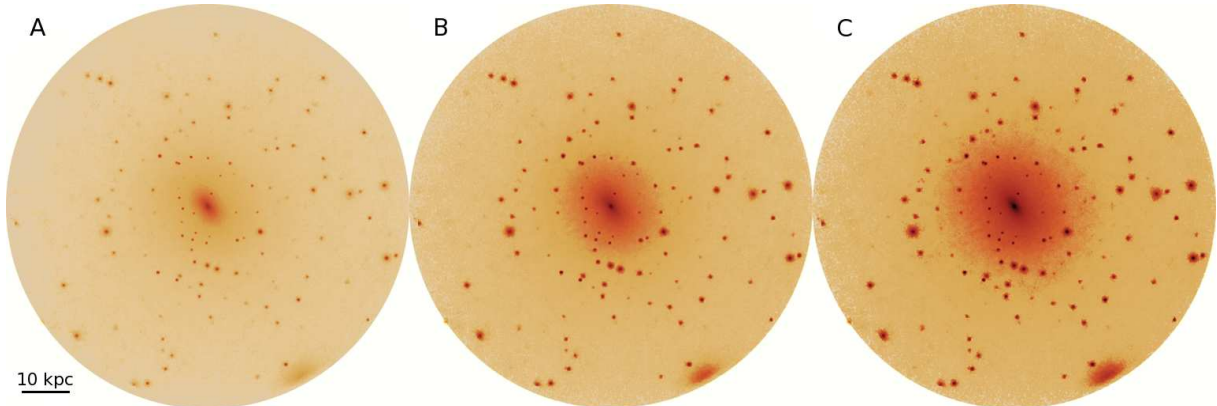


Figure 3: Annihilation rate maps (projections of $\rho^2 S$ out to the tidal radius) of one of the most massive ($M \sim 2 \times 10^9 M_\odot$) subhalos in *Via Lactea II*, for the same models as in Fig. 2. The images have not been normalized. Compared to the $S = 1$ case (A), the total luminosity is 2,200 and 160,000 higher for $S \sim 1/v$ (B) and $S \sim 1/v^2$ (C), respectively.

rate, this “temperature inversion” leads to a relative brightening of the center at the expense of the diffuse flux from the surrounding region (Fig. 3). The subhalo exhibits its own population of subclumps, also Sommerfeld-enhanced.

To address quantitatively the detectability of Sommerfeld-enhanced subhalos by the *Fermi* Space Telescope, we have converted the annihilation flux calculated from our simulation (30) into a predicted γ -ray flux and compared it to the expected backgrounds. We investigated two different classes of particle physics models (Table 1):

- i) those motivated by (10), in which the force carrier is the conventional weak force gauge boson, the W or Z particle, and the mass of the dark matter particle is $\gtrsim 4$ TeV. We have chosen four representative values of m_χ and α , which lie increasingly close to a $S \sim 1/v^2$ resonance. In these models the main source of γ -rays is the decay of neutral pions that are produced in the hadronization of the annihilation products;
- ii) and those in which the annihilation is mediated by a new dark sector force carrier ϕ (11). The choice of parameters (m_χ, m_ϕ, α) follows Meade, Papucci, & Volansky (MPV) (31) and satisfies constraints from recent H.E.S.S. measurements of the Galactic Center (32) and the Galactic Ridge (33), as well as the PAMELA measurement of the local positron fraction above 10 GeV (12) and the ATIC (13) and PPB-BETS (14) measurements of the total $(e^+ + e^-)$ flux above 100 GeV. Models MPV-1 incorporate all three constraints and models MPV-2 only the H.E.S.S. and PAMELA data. We considered models away from (a) and close to (b) resonance, thereby covering both $S \sim 1/v$ and $\sim 1/v^2$ behavior. The data favor a light force carrier, $m_\phi \approx 200$ MeV, and the γ -rays originate then as final state radiation (internal bremsstrahlung) accompanying the decay of the ϕ 's into e^+e^- pairs.

The magnitude of the relativistic cross section was fixed to the standard value of $\langle\sigma v\rangle_0 = 3 \times 10^{-26} \text{ cm}^3 \text{ s}^{-1}$. γ -ray spectra are shown in Figure S2 in the Supporting Online Material.

Table 1: Summary of the models used to assess subhalo detectability with *Fermi*. Particle physics parameters are: m_χ , the mass of the dark matter particle, m_ϕ , the mass of the force carrier, and α , the coupling constant. In the two right-most columns we give S_{\max} , the maximum Sommerfeld enhancement obtained, and the saturation velocity v_{sat} , defined as the velocity at which S reaches 90% of S_{\max} .

Model	m_χ (TeV)	m_ϕ (GeV)	$\alpha \times 100$	S_{\max}	v_{sat} (km s ⁻¹)
LS-1	4.30	90	3.307	1,500	80
LS-2	4.45	90	3.297	12,000	28
LS-3	4.50	90	3.288	70,000	12
LS-4	4.55	90	3.281	430,000	4.7
MPV-1a	1.0	0.2	4.000	3,000	7.4
MPV-1b	1.0	0.2	3.739	16,000	2.4
MPV-2a	0.25	0.2	4.000	480	40
MPV-2b	0.25	0.2	4.500	40,000	3.3

We determined the *Fermi* detection significance by summing the annihilation photons from all the pixels in our all-sky maps covering a given subhalo, and compared this to the square root of the number of background photons from the same area. We counted a subhalo as “detectable” if it had a total signal-to-noise greater than 5 (Table 2). The numbers are quite large, implying that individual subhalos should easily be detected by *Fermi* if Sommerfeld enhancements are important. Even in the most conservative cases (MPV-1a and MPV-2a) around ten or more subhalos should be discovered after 5 years of observation. In fact, on the basis of all models considered here it is predicted that *Fermi* should be able to accumulate enough flux in its first year of observations to detect several dark matter subhalos at more than 5σ significance, a prediction that will soon be tested, and that may open up the door to studies of non-gravitational dark matter interactions and new particle physics. The central brightening discussed above results in a smaller angular extent of a given subhalo’s detectable region: the stronger the Sommerfeld enhancement the fewer pixels exceed the detection threshold. Nevertheless, for all models considered here the majority of detectable subhalos would be resolved sources for *Fermi*.

Another question of interest is whether Sommerfeld-corrected substructure would lead to a significant boost in the local production of high energy positrons, arising from dark matter annihilation in subhalos within a diffusion region of a few thousand parsecs from Earth, as well as of antiprotons within a correspondingly larger diffusion region. The local dark matter distribution at the Sun’s location appears quite smooth in the highest-resolution numerical simulations to date (27, 29, 34). Tidal forces efficiently strip matter from subhalos passing close to the Galactic Center and often completely destroy them. Further substructure depletion may be expected from interactions with the stellar disk and bulge. In the *Via Lactea II* simulation, the mean number of $> 10^5 M_\odot$ subhalos within 1 kpc of the Sun is only 0.04, and one must reach three times farther to find one clump on average. Without the Sommerfeld effect, this dearth of nearby substructure leads to a local annihilation boost of less than 1%, and at most

Table 2: Detectable Subhalos. The number of subhalos that would be detected with $> 5\sigma$ significance by *Fermi* after 1, 2, 5, and 10 years in orbit, for different Sommerfeld-enhanced dark matter particle models. In the two right-most columns we give the median distance and mass of the detectable clumps after 5 years in orbit.

Model	1 yr	2 yr	5 yr	10 yr	\tilde{D} (kpc)	\tilde{M}_{sub} (M_{\odot})
LS-1	12	19	29	38	24	1.4×10^7
LS-2	72	99	167	244	42	9.5×10^6
LS-3	225	311	457	583	56	6.2×10^6
LS-4	410	528	730	919	66	4.9×10^6
MPV-1a	5	7	12	15	16	9.8×10^7
MPV-1b	9	14	25	36	25	4.4×10^6
MPV-2a	12	18	29	38	24	1.4×10^7
MPV-2b	187	254	397	518	55	4.5×10^6

20% in the rare case of a nearby clump, as found in a statistical approach (35). The picture changes with Sommerfeld enhancement. The low velocity dispersion of cold substructure leads to a greatly increased luminosity compared to the hotter smooth component. For typical $1/v$ models, subhalos resolved in our simulation within 2 kpc contribute on average about half as much luminosity as the smooth component, and up to 5 times as much in rare cases. If the Sommerfeld enhancement is resonant ($S \sim 1/v^2$), then these subhalos dominate by a factor of 20 on average and by as much as 200 in rare cases.

References and Notes

1. G. Jungman, M. Kamionkowski, K. Griest, *Phys. Rep.* **267**, 195 (1996)
2. A. Klypin, A. V. Kravtsov, O. Valenzuela, F. Prada, *Astrophys. J.* **522**, 82 (1999)
3. B. Moore, S. Ghigna, F. Governato, G. Lake, T. Quinn, J. Stadel, P. Tozzi, *Astrophys. J. Lett.* **524**, 19 (1999)
4. J. Diemand, M. Kuhlen, P. Madau, *Astrophys. J.* **657**, 262 (2007)
5. J. Silk, M. Srednicki, *Phys. Rev. Lett.* **53**, 624 (1984)
6. M. Kuhlen, J. Diemand, P. Madau, *Astrophys. J.* **686**, 262 (2008)
7. L. Pieri, G. Bertone, E. Branchini, *Mon. Not. R. Astron. Soc.* **384**, 1627 (2008)
8. J. Hisano, S. Matsumoto, M. M. Nojiri, *Phys. Rev. Lett.* **92**, 031303 (2004)
9. J. March-Russell, S. M. West, *Phys. Lett. B* **676**, 133 (2009)

10. M. Lattanzi, J. Silk, *Phys. Rev. D* **79**, 083523 (2009)
11. N. Arkani-Hamed, D. P. Finkbeiner, T. R. Slatyer, N. Weiner, *Phys. Rev. D* **79**, 015014 (2009)
12. O. Adriani, et al., submitted to *Nature* (available at <http://arxiv.org/abs/0810.4995>) (2008)
13. J. Chang, et al., *Nature* **456**, 362 (2008)
14. S. Torii, et al., submitted to *Astropart. Physics* (available at <http://arxiv.org/abs/0809.0760>) (2008)
15. A. A. Abdo, et al., *Phys. Rev. Lett.*, **102**, 181101 (2009)
16. H.E.S.S. Collaboration: F.Aharonian, et al., *preprint* (available at <http://arxiv.org/abs/0905.0105>) (2009)
17. S. Profumo, *preprint* (available at <http://arxiv.org/abs/0812.4457>) (2009)
18. N. J. Shaviv, E. Nakar, T. Piran, *preprint* (available at <http://arxiv.org/abs/0902.0376>) (2009)
19. D. Malyshev, I. Cholis, J. Gelfand, submitted to *Phys. Rev. D* (available at <http://arxiv.org/abs/0903.1310>) (2009)
20. L. Bergström, J. Edsjö, G. Zaharijas, *preprint* (available at <http://arxiv.org/abs/0905.0333>) (2009)
21. P. Meade, M. Papucci, A. Strumia, T. Volansky, *preprint* (available at <http://arxiv.org/abs/0905.0480>) (2009)
22. M. Kuhlen, D. Malyshev, *Phys. Rev. D* **79**, 123517 (2009)
23. M. Cirelli, M. Kadastik, M. Raidal, A. Strumia, *Nucl. Phys. B* **813**, 1 (2009)
24. The “dark sector” of our universe consists of dark matter, dark energy, and possibly additional dark forces.
25. B. E. Robertson, A. R. Zentner, *Phys. Rev. D*, **79**, 083525 (2009)
26. J. Bovy, *Phys. Rev. D* **79**, 083539 (2009)
27. J. Diemand, M. Kuhlen, P. Madau, M. Zemp, B. Moore, D. Potter, J. Stadel, *Nature* **454**, 735 (2008)
28. P. Madau, M. Kuhlen, J. Diemand, B. Moore, M. Zemp, D. Potter, J. Stadel, *Astrophys. J. Lett.* **689**, 41 (2008)

29. M. Zemp, J. Diemand, P. Madau, M. Kuhlen, B. Moore, D. Potter, J. Stadel, L. Widrow, *Mon. Not. R. Astron. Soc.* **394**, 641 (2009)
30. Even at the extremely high resolution of *Via Lactea II* the cuspy subhalo centers are often not sufficiently well resolved to give accurate central surface brightnesses. We corrected the centers according to an analytical model that has been calibrated to our numerical simulations (see Supporting Online Material).
31. P. Meade, M. Papucci, T. Volansky, *preprint* (available at <http://arxiv.org/abs/0901.2925>) (2009)
32. F. Aharonian, et al., *Phys. Rev. Lett.* **97**, 221102 (2006)
33. F. Aharonian, et al., *Nature* **439**, 695 (2006)
34. M. Vogelsberger, et al., *Mon. Not. R. Astron. Soc.* **395**, 797 (2009)
35. J. Lavalley, Q. Yuan, D. Maurin, X. Bi, *Astron. Astrophys.* **479**, 427 (2008)
36. Support for this work was provided by NASA through grant NNX08AV68G (P.M.) and by the William L. Loughlin Fellowship at the Institute for Advanced Study (M.K.). This work would not have been possible without the expertise and invaluable contributions of all the members of the Via Lactea Project team. We thank M. Lattanzi, S. Profumo, N. Arkani-Hamed, N. Weiner, P. Meade and T. Volansky for enlightening discussions, D. Shih for help with the Sommerfeld enhancement calculations, and M. Papucci for providing γ -ray spectra.

Supporting Online Material

www.sciencemag.org

Supporting text

Figs. S1, S2, S3, S4, S5, S6

Supporting Online Material

“Exploring Dark Matter with Milky Way substructure”

Kuhlen, Madau, & Silk

S1 Sommerfeld enhancement

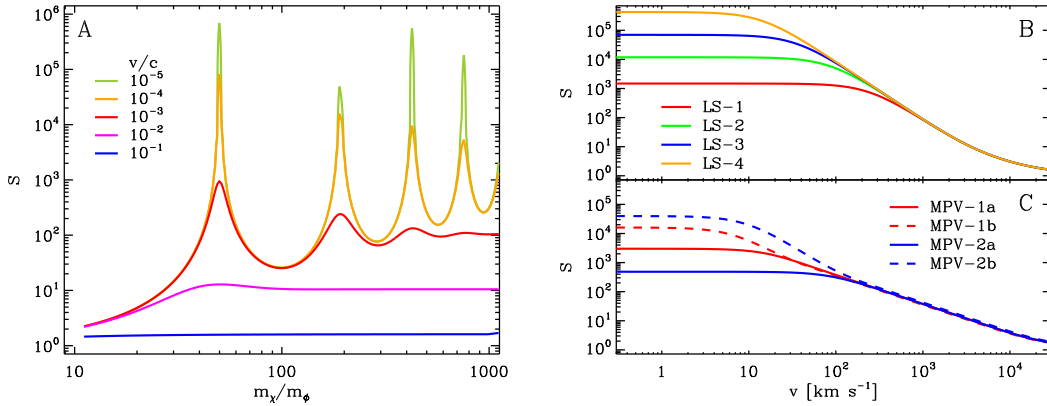


Figure S1: A: The Sommerfeld enhancement factor S as a function of m_χ/m_ϕ (the mass ratio of the dark matter particle to the force carrier particle) at a fixed coupling ($\alpha = 0.30$) for different velocities. B and C: S as a function of velocity for the models for which we calculate subhalo detectability with *Fermi*. The parameters of the models are given in Table 1 in the main text.

A Sommerfeld enhancement to the annihilation cross-section arises when the dark matter (DM) particle is heavy compared to the gauge boson mediating the interaction: $m_\chi \gtrsim m_\phi/\alpha$, where $\alpha = \lambda^2/4\pi$, and λ is the coupling between the dark matter particle χ and the force carrier ϕ . The magnitude of the enhancement can be determined by solving the two-body radial Schrödinger equation, as shown in (1, 2). Defining the additional dimensionless parameter

$$\beta^* = \sqrt{\frac{\alpha m_\phi}{m_\chi}}, \quad (1)$$

one can distinguish three regimes for the dependence of the enhancement S as a function of the velocity (2):

- i) for large velocities, $\beta \equiv v/c \gg \alpha$, there is no Sommerfeld enhancement, $S \sim 1$. This ensures that the relic abundance of dark matter is not affected, since the velocities were close to relativistic at freeze-out;
- ii) at intermediate velocities, $\beta^* \ll \beta \ll \alpha$, the Sommerfeld enhancement follows a $1/v$ behavior, $S \approx \pi\alpha/\beta$;

- iii) at low velocities, $\beta \ll \beta^*$, resonances appear for certain values of m_χ , due to the presence of bound states. In this case S grows as $1/v^2$ before saturating at a velocity that depends on how close to resonance m_χ lies. In the non-resonant case the Sommerfeld enhancement saturates when the deBroglie wavelength of the particle $\sim (m_\chi v)^{-1}$ becomes comparable to the range of the interaction $\sim m_\phi^{-1}$, i.e. when $v \sim m_\phi/m_\chi$.

Figure S1 shows the rich behavior of the Sommerfeld enhancement, obtained by numerical integration of the Schrödinger equation with a Yukawa potential.

The magnitude of the Sommerfeld enhancement at a given location depends on the details of the distribution of relative velocities of the DM particles. Accurately determining the phase-space structure as a function of position is a notoriously difficult task even with the highest resolution N-body simulations. Some recent investigations based on cosmological N-body simulations have found significant structure in the coarse-grained velocity distribution of the host halo and departures from a simple, single-“temperature” Maxwell-Boltzmann distribution (3, 4). These features are remnants of the accretion history of the host halo due to incomplete phase mixing. The centers of subhalos, however, are likely more well-mixed and may show less significant departures from a Maxwellian. At any rate, a full characterization of the phase-space distribution at all locations in our simulation is beyond the scope of this paper, and hence we make the simplifying assumption that the distribution of relative velocities is of the Maxwell-Boltzmann form

$$f(v_{\text{rel}}; \sigma_{\mu,1\text{D}}) = 4\pi \frac{1}{(2\pi\sigma_{\mu,1\text{D}})^{3/2}} v_{\text{rel}}^2 \exp\left[-\frac{1}{2}\left(\frac{v_{\text{rel}}}{\sigma_{\mu,1\text{D}}}\right)^2\right], \quad (2)$$

with a one-dimensional velocity dispersion

$$\sigma_{\mu,1\text{D}}^2 \equiv \frac{kT}{\mu} = 2\frac{kT}{m} = 2\sigma_{m,1\text{D}}^2, \quad (3)$$

where $\mu = m_1 m_2 / (m_1 + m_2) = m/2$ is the reduced mass of a two particle system. From the simulated particles we determine a three-dimensional velocity dispersion, $\sigma^2 \equiv \sigma_{m,3\text{D}}^2 = 3\sigma_{m,1\text{D}}^2 = 3/2\sigma_{\mu,1\text{D}}^2$ (for systems with zero velocity anisotropy). The Maxwell-Boltzmann-weighted Sommerfeld enhancement is then given by

$$S(\sigma) = \int_0^\infty f(v; \sqrt{2/3}\sigma) S(v) dv. \quad (4)$$

S2 Gamma-rays from dark matter annihilation

Since the dark matter particle is neutral it does not couple directly to the electromagnetic field, and hence annihilations straight into two monochromatic photons (or a photon and a Z boson) are typically strongly suppressed. Nevertheless γ -rays can be a significant by-product of dark matter annihilations, since they can arise either from the decay of neutral pions produced in

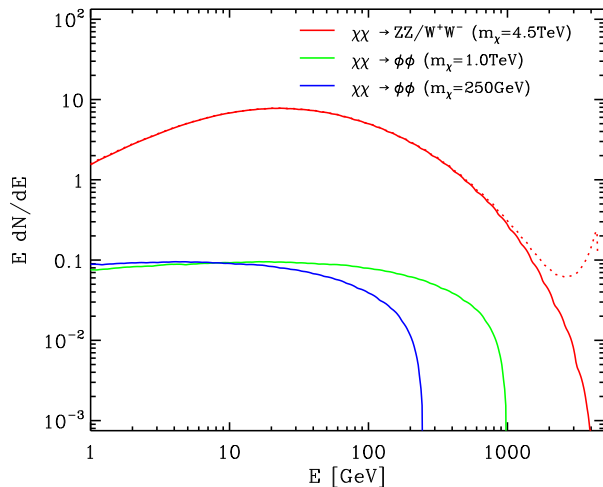


Figure S2: The γ -ray spectrum per annihilation for the models under consideration here. In the LS models ($\chi\chi \rightarrow ZZ$ or W^+W^-) the γ -rays come from the decay of pions produced in the decay of the bosons. The dotted line indicates the internal bremsstrahlung contribution in the case of W^+W^- (5). In the MPV models ($\chi\chi \rightarrow \phi\phi$) the γ -rays originate as final state radiation associated with the decay of the ϕ carriers into e^+e^- pairs.

the hadronization of the annihilation products, or through internal bremsstrahlung associated with annihilations into charged particles, or from interactions of energetic leptons with the surrounding interstellar photons (inverse Compton scattering). We do not consider the latter process here, since we are focusing on the annihilation signal from dark matter subhalos which are unlikely to harbor a sufficiently high stellar radiation field.

The γ -ray spectra per annihilation that we use in our detectability calculation are shown in Figure S2. In the Lattanzi & Silk models the annihilation results in two neutral Z bosons or a pair of W^+ and W^- bosons, and the dominant source of γ -rays is neutral pion decay. For $m_\chi = 4.5$ TeV, every annihilation results in ~ 26 photons with energies between 3 and 300 GeV. In the MPV models, the mass of the ϕ particle is so low (by design), that only decays into e^+e^- pairs are kinematically allowed, and we must rely on final state radiation (internal bremsstrahlung) for the γ -ray signal. This results in fewer 3-300 GeV γ -rays per annihilation (0.39 for $m_\chi = 1$ TeV, 0.30 for $m_\chi = 250$ GeV), but this is partially compensated by the smaller dark matter particle mass and hence higher number density at fixed mass density.

S3 The velocity structure of the Via Lactea II host and its subhalos

In Figure S3 we present radial profiles of the density ρ , velocity dispersion σ , and velocity anisotropy parameter β for the smooth host halo and averaged over the 100 most massive sub-

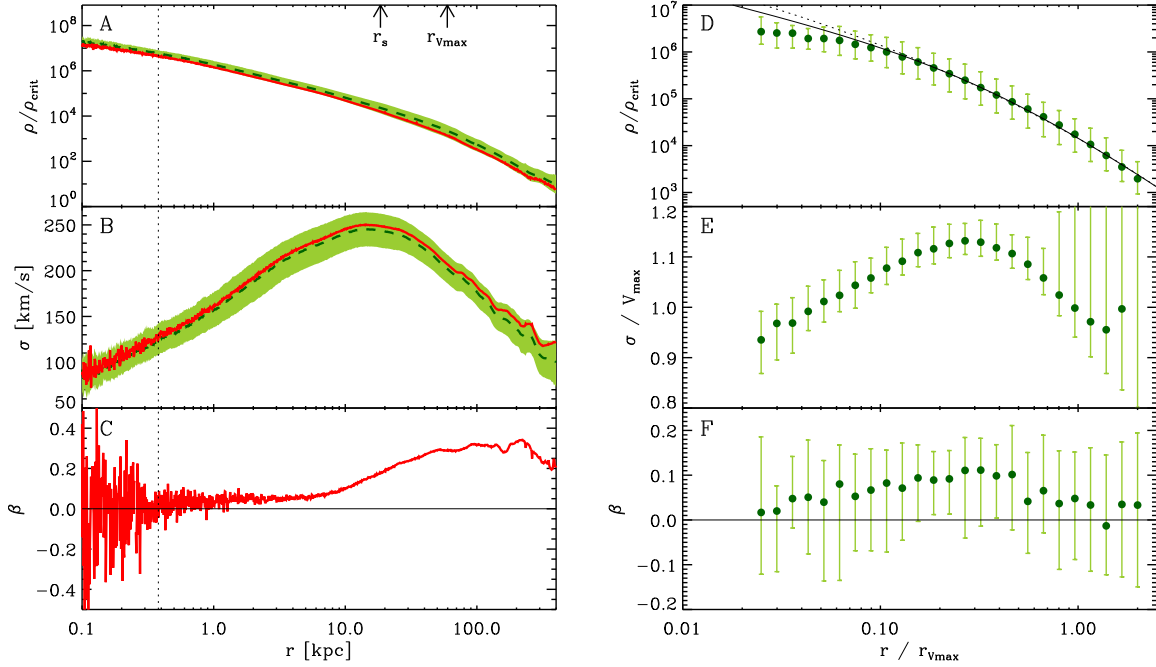


Figure S3: *Left panel:* The radial dependence of the density (A), velocity dispersion (B), and the velocity anisotropy $\beta = 1 - \frac{1}{2} \frac{\sigma_\theta^2 + \sigma_\phi^2}{\sigma_r^2}$ (C) for the smooth host halo component. The solid red line shows the values calculated from all particles in spherical shells. For the ρ and σ profiles we also show the median (dark green dashed line) and the 68% region (light green shaded region) of the particle-by-particle quantities determined from the nearest 32 neighbors. The vertical dashed line indicates our estimate for the convergence radius of the density profile (380 pc). The shape of the σ profile implies that Sommerfeld enhancement will preferentially brighten the very central region of the host halo at the expense of the surrounding region. The anisotropy profile clearly shows that the host halo is not isotropic, with a slight radial anisotropy persisting down to the convergence radius. *Right panel (D-F):* The same quantities averaged over the 100 most massive subhalos. The bullets indicate the median and the error bars the 68% scatter around the median. In D and E we also plot the best-fitting NFW (solid) and Einasto (α fixed at 0.17, dotted) profiles. Note that the subhalo profiles should not be considered converged below $\sim 0.1 r_{\text{Vmax}}$.

halos. We determine these profiles by first binning all particles into equally spaced logarithmic radial shells, and then calculating

$$\rho(r) = \frac{\sum_i m_i}{4\pi r^2 dr}, \quad (5)$$

$$\sigma_j^2(r) = \langle (v_j - \langle v_j \rangle_i)^2 \rangle_i, \quad (6)$$

$$\sigma^2(r) = \sigma_x^2(r) + \sigma_y^2(r) + \sigma_z^2(r), \quad (7)$$

$$\beta(r) = 1 - \frac{1}{2} \frac{\sigma_\theta^2(r) + \sigma_\phi^2(r)}{\sigma_r^2(r)}, \quad (8)$$

where the sum and averages (denoted by $\langle \rangle_i$) are over all particles in a given spherical shell. These profiles are indicated by the solid red line for the host halo in the left panels of Figure S3. For the $\rho(r)$ and $\sigma(r)$ profiles we also show the median and 68% interval of the distribution of particle density ρ_i and velocity dispersion σ_i , both calculated from the 32 nearest neigh-

boring particles. The two estimates agree quite well with each other, with the slightly higher (lower) median ρ_i (σ_i) indicating a negative (positive) skew of the distribution, presumably due to spherical averaging of a triaxial mass distribution. Since 32 particles are not sufficient for a good estimate of β , we don't show the distributions for the velocity anisotropy.

The density profile of the *Via Lactea II* host has been discussed in (6) and we present it here merely for completeness. Down to our convergence radius of 380 pc it is well fit by a generalized NFW profile,

$$\rho(r) = \frac{\rho_s 2^{3-\gamma}}{(r/r_s)^\gamma (1 + r/r_s)^{3-\gamma}}, \quad (9)$$

with a central slope of $\gamma = 1.2$, but an Einasto profile,

$$\rho(r) = \rho_s \exp \left[-\frac{\alpha}{2} ((r/r_s)^\alpha - 1) \right], \quad (10)$$

with $\alpha = 0.167$ fits almost as well. The velocity dispersion profile exhibits the central “temperature inversion” typical of cold dark matter halos: $\sigma(r)$ peaks at about the scale radius and decreases with decreasing radius (7–9). The $\beta(r)$ profile shows the well established trend of a considerable amount of radial anisotropy in the outskirts of the halo and decreasing towards the center (7–9). We find that even at the convergence radius a slight amount of radial anisotropy remains.

In the right panels of Figure S3 we show the ρ , σ , and β profiles averaged over the 100 most massive subhalos in our simulations. We scaled the radius of each subhalo by its $r_{V_{\max}}$ and calculated radial profiles using 30 equally spaced logarithmic bins from $r/r_{V_{\max}} = 0.01$ to 2. In each radial bin we then determined the median and 68% region of the distribution of values over all 100 subhalos, rejecting bins containing less than 100 particles. We only plotted bins containing values from more than 10 subhalos. It is difficult to estimate a convergence radius for these subhalos; the host halo convergence radius of 380 pc corresponds to (0.05 - 0.5) $r_{V_{\max}}$ for these 100 subhalos, so these average profiles should not be considered converged below $\sim 0.1 r_{V_{\max}}$.

The median density profile nicely follows the anticipated NFW-like profile. We have overplotted the best-fitting NFW (solid line) and Einasto (with fixed $\alpha = 0.17$, dotted line) profiles. Clearly the resolution is not good enough to allow a quantitative analysis of the asymptotic central slope of the density profile, but it remains cuspy as far down as we can resolve. The velocity dispersion profile looks qualitatively the same as the host halo's, with a peak around $0.25 r_{V_{\max}}$ and decreasing towards smaller radii. Not surprisingly, subhalos are not isothermal. The strong increase in the 84th percentile of σ at large radii is due to contamination by host halo particles which artificially inflate σ . Although the β profile is quite noisy, it is clear that subhalos too exhibit a slight radial anisotropy even down at the smallest radii that we can access.

An important caveat to these findings is that our simulations completely neglect the effects of baryons on the DM distribution. Gas cooling, star formation, supernova feedback, and stellar dynamical processes might alter both the DM density and velocity dispersion profiles. In fact, not even the sign of these effects is clear at the moment: adiabatic contraction generally leads

to a steepening of the central density profile (10, 11), but dynamical friction acting on baryonic condensations tends to remove the central cusp (12, 13). The velocity dispersion of DM particles, on the other hand, is more likely to increase in regions affected by baryonic processes. These complications will be most important for the Galactic Center. The high mass-to-light ratios observed in Galactic dwarf satellites (14) indicate that they are completely DM dominated and hence likely much less affected by baryonic physics. Interactions with the Milky Way’s stellar and gaseous disk probably strip a significant fraction of mass from some DM subhalos, but the dense central regions responsible for most of the annihilation luminosity are relatively well protected.

S4 Detectability Calculation

We calculated the annihilation flux directly from our simulations following the procedure detailed in (16), with one important modification to account for the Sommerfeld enhancement. The intensity in a given direction (θ, ϕ) is now given by

$$\mathcal{I}(\theta, \phi) = \mathcal{G} \int_{\text{los}} \rho^2 S(\sigma; m_\chi, m_\phi, \alpha) d\ell, \quad (11)$$

where \mathcal{G} contains most of the particle physics dependence (the particle mass, the high velocity annihilation cross section, and the γ -ray spectrum per annihilation event) and $S(\sigma; m_\chi, m_\phi, \alpha)$ is the Maxwell-Boltzmann-weighted Sommerfeld enhancement factor at a velocity dispersion σ for a given particle physics model. For discrete particles, with masses m_i , distances d_i , densities ρ_i , and velocity dispersions σ_i , this integral becomes a discrete sum over all particles in a given map pixel,

$$\sum_i \frac{\rho_i S(\sigma_i) m_i}{4\pi d_i^2}. \quad (12)$$

We determined ρ_i and σ_i from the nearest 32 neighbors of the i th particle, but have checked that our results do not change significantly for 64 neighbors. We have implemented several additional improvements over (16): (a) we corrected a calculation error in the conversion from simulation fluxes to gamma-ray counts (the subhalo fluxes were a factor of two too large in (16)), (b) we use a 15% lower effective area ($\sim 7,300 \text{ cm}^2$), as suggested by the performance of the LAT instrument measured in orbit (17), and (c) we switched to the HEALPix¹ equal area pixelization scheme, setting $N_{\text{side}} = 512$, which corresponds to a solid angle per pixel of $\Delta\Omega = 4 \times 10^{-6}$ sterad, comparable to the angular resolution of *Fermi*’s LAT detector above 3 GeV. We assumed a LAT exposure time equal to 0.153 of the time in orbit, a combination of the $\sim 4\pi/5$ sr field of view, 90% trigger live time, and 15% data acquisition outage during South Atlantic Anomaly passages (17). Our analysis was restricted to one fiducial observer located at 8 kpc from the host halo center along the intermediate axis of its density ellipsoid, and we

¹<http://healpix.jpl.nasa.gov/>

refer the reader to (16) for a discussion of the signal variance arising from different observer locations.

Due to the finite resolution of our simulation the centers of all our halos are artificially heated and less dense than they would be at higher resolution. This results in central brightnesses that are lower than would be expected for an NFW or Einasto density profile. We have corrected the central flux from the host halo and all subhalos using an analytical extrapolation of the density and velocity dispersion profiles. We considered both an NFW ($\gamma = 1$) profile and an Einasto profile with $\alpha = 0.17$, which has been shown to fit Galactic-scale dark matter halos (18). These analytical profiles are matched to the measured values of V_{\max} and $r_{V\max}$, which are robustly determined for subhalos with more than 200 particles ($M > 8 \times 10^5 M_{\odot}$). The relations between $(V_{\max}, r_{V\max})$ and (ρ_s, r_s) are

$$r_{V\max} = f_r r_s \quad V_{\max}^2 = f_V 4\pi G \rho_s r_s^2, \quad (13)$$

with $f_r \approx 2.163$ (2.212) and $f_V \approx 0.865$ (0.897) for the NFW (Einasto) profile. We use the spherical Jeans equation to solve for the corresponding velocity dispersion profile, assuming $\beta = 0$. For a halo at a given distance we can then solve for a Sommerfeld-enhanced surface brightness profile as a function of angle from the halo center, average it over the angular resolution of our maps ($\Delta\Omega = 4 \times 10^{-6}$ sterad), and use this to correct our simulated maps. For the host halo we only correct pixels within $\sim 2.7^\circ$ from the center, corresponding to the density profile convergence radius of 380 pc. For the subhalos we ensure that all pixels within the projected scale radius r_s have a surface brightness at least as high as the expectation from the analytical extrapolation. These correction factors are typically not very large: over all subhalos and all Sommerfeld models, the median (root mean square) correction factor for the central pixel is 2.2 (5.0).

Note that we neglect the possible enhancement of a subhalo’s luminosity arising from additional clumpy substructure below our simulation’s resolution limit. The magnitude of this so-called “substructure boost factor” depends on uncertain extrapolations of the abundance, distribution, and internal properties of the low mass subhalos, and will not be significantly increased by the Sommerfeld effect due to its saturation at low velocities. While this boost typically doesn’t affect the central surface brightness very much, it may somewhat increase the angular extent of a given subhalo’s signal.

The annihilation signal from individual subhalos must compete with a number of diffuse γ -ray backgrounds, of both astrophysical and DM annihilation origin. At low Galactic latitudes the dominant astrophysical background arises from the interaction of high energy cosmic rays with interstellar gas (pion decay and bremsstrahlung) and radiation fields (inverse Compton). This background has been measured by the EGRET instrument aboard the Compton satellite at 0.5 degree resolution out to ~ 30 GeV (19). An improved measurement of the spectral and angular properties of this background is one of the goals of the *Fermi* mission, and preliminary data at intermediate Galactic latitudes have already been presented by the Fermi collaboration (20). Here we employ a theoretical model of this background (the GALPROP “conventional” model (21, 22)), which matches the EGRET and preliminary Fermi measure-

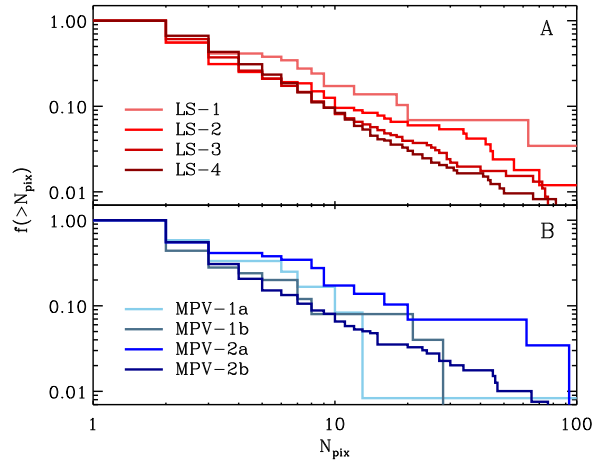


Figure S4: Cumulative distribution of the angular size of the detectable subhalos. We plot the fraction of $S/N > 5$ subhalos with more than N_{pix} pixels exceeding the *Fermi* detection threshold after 5 years in orbit, for the LS models in panel A, and for the MPV models in panel B.

ments with sufficient accuracy for our purposes. At high Galactic latitudes ($|b| \gtrsim 20^\circ$), an isotropic extragalactic γ -ray background from unresolved blazars may become dominant. We include such a background with an intensity and spectrum as measured by EGRET (23). Note that this is probably an overestimate, since *Fermi* will likely resolve some fraction of this background into point sources. We do not include the contributions from astrophysical foreground and background point sources, but we have checked that none of the Sommerfeld-enhanced subhalos would have been detected by EGRET, assuming a point-source sensitivity of $2 \times 10^{-7} \gamma \text{ cm}^2 \text{ s}^{-1}$ from 0.1 to 30 GeV (24).

In addition to these astrophysical backgrounds, individually detectable subhalos must compete with the diffuse background from DM annihilation in the smooth host halo and from the population of individually undetectable subhalos (see Section S5) (16, 25). In models without Sommerfeld enhancement and for $S \sim 1/v$ models, these DM annihilation backgrounds are negligible compared to the astrophysical backgrounds (although they themselves constitute a signal worth searching for). In resonant $S \sim 1/v^2$ models with low saturation velocity (e.g. LS-3, LS-4, MPV-1b, MPV-2b), however, the unresolved subhalo flux becomes the dominant background and must be accounted for. For completeness we have included all four components in the detectability calculation in all cases.

Subhalo detectability for *Fermi* is assessed as follows. First we calculate a signal-to-noise ratio (S/N) *per pixel* by dividing the number of source photons arising in the subhalo map by the square root of the number of photons in the background map. Next we select all pixels with $S/N > 1$ and identify contiguous regions, which we associate with individual subhalos based on proximity of the brightest pixel with a subhalo center. If more than one subhalo center coincides with a given brightest pixel, we pick the subhalo with the larger expected surface brightness ($L/r_s^2 \sim V_{\text{max}}^4/r_{\text{Vmax}}^3$). For each of these contiguous regions we then calculate a

subhalo detection significance

$$S/N = \frac{N_s}{\sqrt{N_b}}, \quad (14)$$

where N_s and N_b are the total number of source and background γ -rays over the contiguous region. This definition is a good proxy for detection significance under the assumption that an estimate of the background can be subtracted out and only Poisson fluctuations remain. Note that it is not the uncertainty of the flux itself (which would be $N_s/\sqrt{N_s + N_b}$), but instead an estimate of the significance of having detected a departure from a smooth background.

In Figure S4 we show the cumulative distribution of the angular size (the number of pixels exceeding the *Fermi* detection threshold after 5 years in orbit) of the detectable subhalos. Although models with stronger Sommerfeld enhancement result in smaller detectable regions, the majority of all subhalos would still be resolved sources for *Fermi*. This effect raises the possibility of future observations being able to discriminate between different Sommerfeld-enhanced models.

S5 Diffuse Flux from Unresolved Subhalos

For a typical CDM power spectrum of density fluctuations one would expect dark matter clumps on scales all the way down to a cutoff set by collisional damping and free streaming in the early universe (26, 27). For WIMP dark matter, typical cut-off masses are $m_0 = 10^{-12}$ to $10^{-4} M_\odot$ (28, 29), some 10 to 20 orders of magnitude below *Via Lactea II*'s mass resolution. In this case the Galactic dark matter halo might host an enormous number ($10^{10} - 10^{22}$, see (16)) of small mass subhalos, whose combined annihilation signal could result in a sizeable γ -ray background. If the Sommerfeld enhancement didn't saturate at a finite velocity, this background would easily outshine any other Galactic γ -ray signal. Even with saturation one must ask whether the Sommerfeld-enhanced annihilation background from this population of unresolved subhalos would outshine individual subhalos.

In order to address this question, we have extended the analytical model of (16) to allow for Sommerfeld enhancement. The overall intensity of this background depends sensitively on a number of uncertain parameters governing the subhalo population as a whole (slope and normalization of the mass function, their dependence on distance to the host center) and the mass dependent properties of individual subhalos (density and velocity dispersion profiles, concentrations). Although the model is calibrated to numerical simulations at the high mass end, it relies on an extrapolation over many orders of magnitude in mass below the simulation's resolution limit that is very uncertain.

Our model employs a radially anti-biased subhalo mass function

$$\frac{dn(M, r)}{dM} = 1.05 \times 10^{-8} M_\odot^{-1} \text{ kpc}^{-3} \left(\frac{M}{10^6 M_\odot} \right)^{-2} \left(1 + \frac{r}{18.5 \text{ kpc}} \right)^{-2} \quad (15)$$

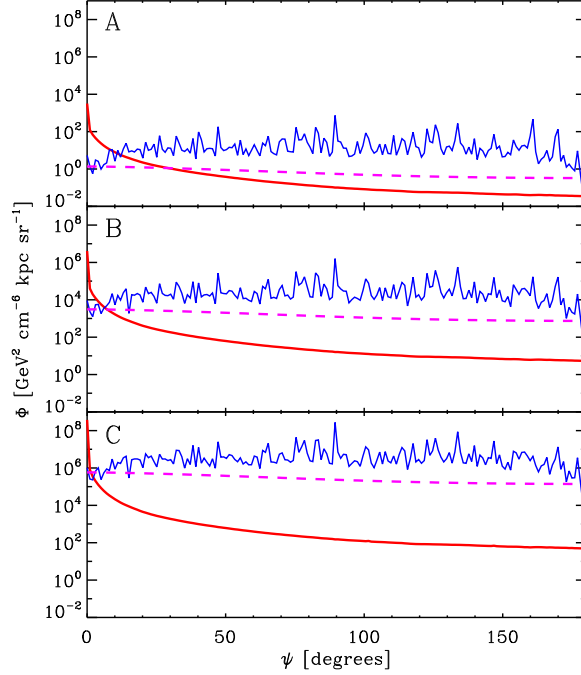


Figure S5: The annihilation intensity as a function of angle ψ from the Galactic Center, for the host halo (red), individual subhalos (blue), and unresolved subhalos (magenta dashed). A: No Sommerfeld enhancement. B: Model MPV-2a ($S \sim 1/v$, high v_{sat}). C: Model LS-4 ($S \sim 1/v^2$, low v_{sat}). For the host halo and unresolved components we plot the *mean*, for the individual subhalo profile the *maximum* intensity over all pixels in a given ψ bin. Individual subhalos outshine the diffuse unresolved subhalo background, even in the strongly Sommerfeld-enhanced case.

with a low mass cutoff of $m_0 = 10^{-6} M_{\odot}$, and assumes an Einasto density and velocity dispersion profile with a concentration-mass relation according to (30) and a radial dependence of

$$c(M, r) = c^{\text{B01}}(M) \left(\frac{r}{400 \text{ kpc}} \right)^{-0.286}. \quad (16)$$

We refer the reader to the Appendix of (16) for details about the calculation. In Figure S5 we show the resulting azimuthally averaged intensity as a function of angle from the Galactic Center, and compare it to the smooth host halo signal and the peaks due to individual subhalos. While the unresolved subhalo background is brighter than the smooth halo component everywhere but in the very center, individual subhalos have higher central surface brightnesses and can easily outshine it. This holds true in all Sommerfeld models that we have considered.

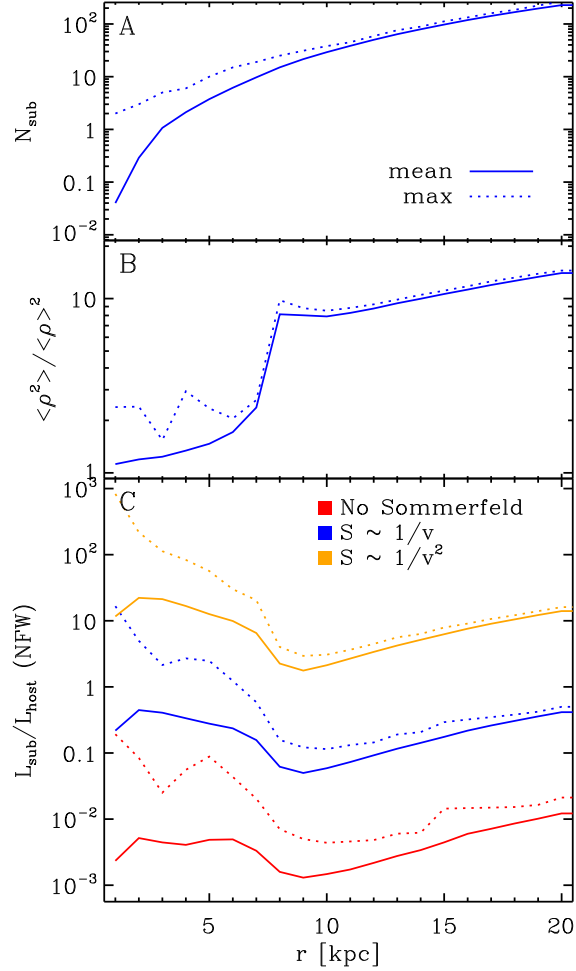


Figure S6: The effect of substructure on the local annihilation rate. A: The mean and maximum number of *Via Lactea II* subhalos inside 100 randomly placed spheres 8 kpc from the halo center versus the radius of these sample spheres. The mean subhalo occupancy becomes unity at $r = 3$ kpc. B: The density “clumping factor” $\langle \rho^2 \rangle / \langle \rho \rangle^2$ over the 100 sample spheres. C: The ratio of the subhalo to host halo contributions to the annihilation luminosity for three representative Sommerfeld models (none, $1/v$, and $1/v^2$). Only subhalos resolved in our simulation are accounted for.

S6 Local Luminosity Boost From Substructure

Here we assess the role that nearby subhalos play for the Sommerfeld-enhanced production of high energy electrons and positrons. Because these energetic particles lose energy as they diffuse through the Galactic magnetic field, only those that are produced within a few kpc of Earth are of interest.

We considered 100 spheres of radius 20 kpc, with randomly positioned centers 8 kpc from

the host halo center. For each of these spheres we determined the cumulative number of subhalos N_{sub} , a “clumping factor”, defined as $\langle \rho^2 \rangle / \langle \rho \rangle^2$, and the ratio of total subhalo to host halo luminosity as a function of enclosed radius in the sphere. For the subhalo luminosity we used the analytical NFW estimate, as explained in Section S4. Figure S6 shows the mean and maximum values of these quantities over all 100 sample spheres. The low local subhalo abundance is reflected in a small mean N_{sub} within a few kpc of the Sun. Only 3 of the 100 sample spheres have any subhalos within 1 kpc of their center. The mean subhalo occupancy becomes unity at 3 kpc, but one has to go out to 7 kpc before every single sphere contains at least one subhalo. The clumping factor captures the enhancement of the annihilation luminosity compared to a homogeneous density background. It has contributions from the overall density stratification, from the Poisson noise of the density estimator, and from unbound and bound substructure. The sharp rise towards 8kpc is due to the cuspy nature of the host halo density profile. The bottom panel of Figure S6 shows that without Sommerfeld enhancements the subhalos do not contribute significantly to the local annihilation luminosity. In a typical $S \sim 1/v$ model, however, subhalos contribute on average about half as much as the host halo, and in rare cases 5 times more. For models on resonance ($S \sim 1/v^2$), the subhalos completely dominate the host halo, and provide on average 20 times as much luminosity as the host halo. Again we have neglected the possible additional contribution from subhalos below our simulation’s resolution limit.

References and Notes

1. N. Arkani-Hamed, D. P. Finkbeiner, T. R. Slatyer, N. Weiner, *Phys. Rev. D* **79**, 015014 (2009)
2. M. Lattanzi, J. Silk, *Phys. Rev. D* **79**, 083523 (2009)
3. M. Vogelsberger, et al., *Mon. Not. R. Astron. Soc.* **395**, 797 (2009)
4. M. Zemp, J. Diemand, P. Madau, M. Kuhlen, B. Moore, D. Potter, J. Stadel, L. Widrow, *Mon. Not. R. Astron. Soc.* **394**, 641 (2009)
5. T. Bringmann, L. Bergström, J. Edsjö, *J. High Energy Phys.* **1**, 49 (2008)
6. J. Diemand, M. Kuhlen, P. Madau, M. Zemp, B. Moore, D. Potter, J. Stadel, *Nature* **454**, 735 (2008)
7. J. Diemand, B. Moore, J. Stadel, *Mon. Not. R. Astron. Soc.* **352**, 535 (2004)
8. M. Hoeft, J. P. Mückel, S. Gottlöber, *Astrophys. J.* **602**, 162 (2004)
9. W. Dehnen, D. E. McLaughlin, *Mon. Not. R. Astron. Soc.* **363**, 1057 (2005)
10. G. R. Blumenthal, S. M. Faber, R. Flores, J. R. Primack, *Astrophys. J.*, **301**, 27 (1986)
11. O. Y. Gnedin, A. V. Kravtsov, A. A. Klypin, & D. Nagai, *Astrophys. J.*, **616**, 16 (2004)
12. A. A. El-Zant, Y. Hoffman, J. R. Primack, F. Combes, I. Shlosman, *Astrophys. J. Lett.*, **607**, 75 (2004)
13. E. Romano-Díaz, I. Shlosman, Y. Hoffman, C. Heller, *Astrophys. J. Lett.* **685**, 105 (2008)
14. J. D. Simon, M. Geha, *Astrophys. J.*, **670**, 313 (2007)
15. M. Kuhlen, J. Diemand, P. Madau, *Astrophys. J.* **671**, 1135 (2007)
16. M. Kuhlen, J. Diemand, P. Madau, *Astrophys. J.* **686**, 262 (2008)
17. R. Johnson, private communication
18. J. F. Navarro, et al., *Mon. Not. R. Astron. Soc.* **349**, 1039 (2004)
19. S. D. Hunter, et al., *Astrophys. J.* **481**, 205 (1997)
20. I. V. Moskalenko, A. W. Strong, *talk at the ENTApP DM workshop 2009* (slides available at <http://indico.cern.ch/materialDisplay.py?materialId=slides&confId=44160>) (2009)
21. A. W. Strong, I. V. Moskalenko, *Astrophys. J.* **509**, 212 (1998)

22. I. V. Moskalenko, A. W. Strong, J. F. Ormes, M. S. Potgieter, *Astrophys. J.* **565**, 280 (2002)
23. P. Sreekumar, et al., *Astrophys. J.* **494**, 523 (1998)
24. R. C. Hartman, et al., *Astrophys. J. Suppl.* **123**, 79 (1999)
25. L. Pieri, G. Bertone, E. Branchini, *Mon. Not. R. Astron. Soc.* **384**, 1627 (2008)
26. A. M. Green, S. Hofmann, D. J. Schwarz, *J. Cosmol. Astropart. Phys.* **8**, 3 (2005)
27. A. Loeb, M. Zaldarriaga, *Phys. Rev. D* **71**, 103520 (2005)
28. S. Profumo, K. Sigurdson, M. Kamionkowski, *Phys. Rev. Lett.* **97**, 031301 (2006)
29. T. Bringmann, submitted to *New Journal of Physics* (available at <http://arxiv.org/abs/0903.0189>) (2009)
30. J. S. Bullock, et al., *Mon. Not. R. Astron. Soc.* **321**, 559 (2001)